Article type: Communication

Electrically and Thermally Tunable Smooth Silicon Metasurfaces for Broadband Terahertz Antireflection

Lu Ding[*]*, Xianshu Luo, Liang Cheng, Maung Thway, Junfeng Song, Soo Jin Chua, Elbert E. M. Chia, Jinghua Teng*[*]

Dr. L. Ding, Dr. J. H. Teng
Institute of Materials Research and Engineering, Agency for Science, Technology and Research (A*STAR), 2 Fusionopolis Way, Innovis, 138634, Singapore
Emails: dingl@imre.a-star.edu.sg; jh-teng@imre.a-star.edu.sg
Dr. X. Luo
Institute of Microelectronics, Agency for Science, Technology and Research (A*STAR), 2 Fusionopolis Way, Innovis, 138634, Singapore
Dr. L. Cheng, Prof. Elbert E. M. Chia
Division of Physics and Applied Physics, School of Physical & Mathematical Sciences, Nanyang Technological University, 637371 Singapore
M. Thway, Prof. S. J. Chua
Department of Electrical and Computer Engineering, National University of Singapore, 11758 Singapore
Prof. J. F. Song
State Key Laboratory on Integrated Opto-Electronics, College of Electronic Science and Engineering, Jilin University, Changchun 130012, People's Republic of China

Keywords: terahertz optics, broadband antireflection, tunable metasurfaces, silicon photonics

The versatile capability of metamaterials and metasurfaces in light manipulation has significant impact on the advancement of terahertz science and technologies.[1, 2] Further development of terahertz technology demands efficient and tunable semiconductor based devices for compact system integration.[3] Here we demonstrate an electrically and thermally tunable silicon metasurface for broadband terahertz antireflection application. The flat silicon metasurface is composed by interdigitated p-n junctions fabricated using a completely complementary metal-oxide-semiconductor (CMOS) compatible process in a silicon photonics foundry. It is atomically smooth without any physically etched pattern nor metal antennas. By supplying bias voltage to *p-n* junctions, complex reflection coefficient of silicon metasurface is continuously tuned between negative and positive values. Antireflection condition can be precisely achieved, proved by the vanishing of the echo pulse in terahertz

time-domain spectroscopy (THz-TDS). The amplitude and phase of the terahertz wave are tuned simultaneously, where the amplitude shows a bias voltage polarity dependence. The active silicon metasurface has a unique property of thermally tuning the reflection while electrically tuning the transmission. The work suggests a new design concept using all-silicon platform for making atomically smooth and electrically controlled metadevices in terahertz and other frequency range.

Metasurfaces are constructed by a thin layer of subwavelength in-plane functional building blocks for manipulating amplitude and phase of the electromagnetic wave.[2] Active metasurfaces, which could be controlled by electrical bias voltage,[4-6] temperature,[7] magnetic field,[8] optical pumping,[9, 10, 11] or mechanical deformation,[12] etc., further extend their designed passive properties by allowing new functionalities or tuning the operational conditions. Recently, various active terahertz metadevices have been demonstrated, such as filters,[9] switches,[6, 11] and modulators via phase,[5] amplitude,[4] and frequency modulation.[10] Versatile functionalities are realized by integrating metasurfaces with functional materials, e.g., graphene,[6] semiconductor two-dimensional electron gas system,[4] and semiconductor hybridized in metamaterial scatterers,[5, 13] etc. Owing to their quasi-planar nature, metasurfaces and metadevices are readily fabricated using planar micro-/nano-patterning techniques, such as lithography, focused ion-beam, and nanoimprinting. Amongst various demonstrations, silicon-based active metadevices are rarely reported despite the facts that silicon is one of the most popular materials used for fabricating terahertz optics and is recently becoming a promising material for metasurface applications.[14] Furthermore, fabrication of silicon-based photonic devices is completely CMOS compatible with merits of large scale manufacturability, low cost, and integration potentials with other photonic architectures.

As one of the important applications, metasurface has been applied to the design of broadband terahertz antireflection coating.[15] Metallic gratings/meshes with deep-subwavelength periodicity have been demonstrated to have ultra-broadband antireflection feature,[16] owing to the flat low-frequency tail of the Drude conductivity of the conductive materials, but with intrinsic tradeoff on resistivity induced transmission loss.[17] The main challenge for all the antireflection coatings is to have the as-fabricated coating precisely matched with the antireflection condition. It can be settled by using an antireflection coating with actively controlled reflection coefficient, which, however, has yet been demonstrated. In this paper, we present a novel atomically smooth silicon metasurface for tunable broadband antireflection application. The design consists of interdigitated p-n junctions, which continuously tunes the complex reflection coefficient of silicon metasurface by supplying bias voltage. Antireflection condition is precisely achieved via impedance matching. The fabrication is CMOS-compatible and scalable using existing silicon photonics fabrication platform. Furthermore, electrical control of the silicon metadevices is simple and direct, which is much favored in the market.

Figure 1a shows schematic of the active silicon antireflection coating. The substrate is double side polished high resistivity float zone silicon (HRFZ Si) which is highly transparent in a broadband terahertz range.[18] Silicon metasurface consists of interdigitated *p*-*n* junctions, namely, alternating *p*- and *n*-type silicon stripes with one dimensional deep-subwavelength periodicity covering the entire surface using ion implantation. One period is composed of one *p*-doped and one *n*-doped stripes with identical width (**Figure 1**b). The *p*- and *n*-type doping has peak concentration of 4×10^{19} cm^{-3} and 7×10^{19} cm^{-3} respectively, and implantation depth of ~ 500 nm (Supporting Information, Figure S1). All *p*- and *n*-doped stripes are separately connected to the corresponding perpendicular *p*++ and *n*++ Ohmic contacts for bias voltage control.

The interdigitated doping pattern is investigated by mid-infrared nano-imaging at 990 cm^{-1} via a scattering-type scanning near-field optical microscope (s-SNOM) (Supporting Information, Figure S2).[19] Atomic force microscope (AFM) topography *z* (**Figure 1**c) and line plot (**Figure 1**d) show no obvious periodicity correlated with the doping pattern. Surface roughness R_a extracted from **Figure 1**d is ~ 0.24 nm. Ion implantation introduces very little surface crystalline damage and the surface is atomically smooth. On the contrary, optical amplitude s_4 and phase φ_4, which are simultaneously attained with *z*, show periodic optical contrast identical to the designed silicon metasurface (**Figure 1**e,g). The optical contrast comes from the difference in complex dielectric function of doped silicon with different doping concentration. Depletion region between p-n junctions is clearly resolved in line plots of s_4 and φ_4 (**Figure 1**f,h), which has a width about 500 ± 50 nm. Phase transition between adjacent doped regions is slightly asymmetric, reflecting a lateral relative shift of 100 nm between *p*- and *n*-type regions. This is attributed to misalignment during two successive ion-implantation process, which corresponds to the alignment accuracy of ± 120 nm.

When a terahertz pulse goes through a silicon substrate, multiple internal reflection (**Figure 2**a) occurs due to the large refractive index difference between silicon (n_{Si} = 3.4175) and air (n_{air} = 1.0003). Fabry-Perot (FP) interference fringes appear in the frequency domain transmission spectrum over a broadband terahertz range, which can be effectively removed by designing active silicon metasurface with bias voltage control. **Figure 2**b shows the amplitude spectra of the transmitted terahertz pulse from the silicon metasurface. The THz-TDS setup is illustrated in Figure S3 (Supporting Information). The device is mounted in TE configuration, where the longer side of silicon stripe parallels with the polarization of the incident terahertz wave. At zero bias, there are obvious FP fringes as seen in the grey curve. FP fringes are eliminated under both reverse and forward biases but with increased (the red curve) and decreased transmission (the blue curve), respectively. In time domain, multiple internal

reflection gives rise to multiple terahertz pulse traces (Supporting Information, Figure S5a). The time difference between two successive pulses is the round trip travelling time of the terahertz pulse in the substrate. **Figure 2**c**,**d plot the evolution of time domain traces of the main pulse P_1 and the first echo pulse P_2 respectively, under the continuously tuning of reverse bias. Precise antireflection condition is indicated by the vanishing of P_2. At 0 V, P_1 and P_2 have phase inverted with each other indicating that the impedance of air has been over compensated by the unbiased silicon metasurface.[20] With increasing reverse bias, P_1 has its amplitude increased and phase delayed, while P_2 has amplitude decreased to about zero at -25 V bias then increased at -40 V bias with phase inversion. The response of device under forward bias (**Figure 2**e,f) is similar to that under reverse bias, except that the amplitude of P_1 decreases. Overall, P_2 is tuned by bias voltage within a range including the precise antireflection condition, regardless of bias polarity. Whereas, the amplitude of P_1 is bias-polarity dependent and the phase of P_1 is simultaneously tuned by bias voltage over a broadband terahertz range.

The device clearly shows a voltage-dependent antireflection behavior with both amplitude and phase of terahertz pulses being continuously tuned. To further understand the origins of the tunability, complex reflection coefficient $\tilde{r_c}$ of silicon metasurface as a function of bias voltage is plotted in **Figure 3**a,b. The amplitude $|r_C|$ and phase φ_C are given by $\tilde{r_c} = |r_c|e^{i\varphi_C} = e^{-i2kL}\, 1/r_{Si}\, (P_2/P_1)$, where e^{-i2kL} is the round trip phase shift in the silicon substrate and L is the thickness of the substrate. In TE configuration, when the absolute value of voltage increases, the amplitude $|r_C|$ continuously decreases till zero and then increases, and the phase φ_C continuously changes from π at zero bias to 0. Precise antireflection condition ($\varphi_C = \pi/2$, red line in **Figure 3**b) is achievable regardless the bias polarity. Here, tuning in $\tilde{r_c}$ is attributed to thermo-optical effect due to Joule heating. With increasing temperature, sheet conductivity of pure *p*- and *n*-doped silicon decreases due to the fact that the mobility is limited by phonon scattering at high temperature: $\mu_{ph} \sim T^{-3/2}$. The impedance mismatching

between silicon and air is then reduced with increasing temperature and the antireflection is achieved. In TM configuration, both $|r_C|$ and φ_C have less dependence on bias voltage (Supporting Information, S8). It is understood that the depletion region blocks the carriers' movement to adjacent doped regions so that terahertz wave is less influenced by the carriers.

Figure 3c plots the current-voltage (*IV*) curve of the active silicon metasurface measured from -47.5 to 27.5 V. The error bar indicates the variation of current at each fixed voltage. The current shows nearly a linear dependence on voltage with slightly different slope for forward and reverse bias. Due to the high doping concentration, the depletion region is very narrow and easily breaks down under reverse bias. Current is mainly limited by series resistance in *n* and *p* regions at large forward and reverse bias. The power conversion from applied electric power (*VI*) to the dissipated power (I^2R) is nearly 100% as shown in the inset of **Figure 3**c. This means that the device is efficiently heated up by electric power when applying bias. **Figure 3**d plots the surface temperature of the device as a function of the dissipated power. Temperature linearly increases with dissipated power in forward and reverse bias at a rate of dT/dP = 13.27 K/W and 15.16 K/W, respectively. The corresponding temperatures to the bias voltage are also indicated in upper *X* axis in **Figure 3**a. The reflection minima fall at temperature around 360 K. The $|r_C|$ calculated with a simplified effective medium model from pure thermal point of view (Supporting Information S7) agrees well with experimental results. Due to the slow thermal response, tuning is 'quasi-static' (Supporting Information S9).

Figure 4a shows the relative time shift of P_1 ($\Delta t_{P_1} = t_{P_1}^{Bias} - t_{P_1}^{0V}$) with respect to the dissipated power. In general, P_1 is linearly dependent on power dissipation and independent on polarization and bias polarity. An error bar of ± 10 fs is included by repeating measurements. Taken slope $\partial t/\partial P$=7.5 fs/W and average Joule heating rate $\partial T/\partial P$=15 K/W, thermo-optic coefficient $\frac{1}{n}\frac{\partial n}{\partial T}$ of silicon is then calculated as 6.1×10^{-5} K^{-1} from relation $\frac{\partial t}{\partial P} =$

$\frac{L}{c}\frac{\partial n}{\partial T}\frac{\partial T}{\partial P}$. It agrees fairly well with reported values.[21] Therefore, Δt_{P_1} is attributed to thermally induced refractive index change in the silicon substrate.

Figure 4b shows the normalized amplitude variation of P_1 ($\Delta A_{P_1}/A_{P_1}^{0V} = \left(A_{P_1}^{Bias} - A_{P_1}^{0V}\right)/A_{P_1}^{0V}$) as a function of bias voltage. $\Delta A_{P_1}/A_{P_1}^{0V}$ is bias polarity dependent with a negative sign to voltage. Total variation of transmission amplitude in TE configuration is ~ 13% between -40 V and +20 V bias voltage. Further increasing voltage results in fast decreasing of $\Delta A_{P_1}/A_{P_1}^{0V}$ which is attributed to the breakdown of *p-n* junctions in reverse bias and unstable IV performance due to overheating in forward bias. The amplitude of transmission coefficient of silicon metasurface can be described as $t(\omega) = \frac{2n_{Si}}{n_{Si}+n_{air}+Z_0 d\tilde{\sigma}(\omega)}$,[20] where d is doping depth, $\tilde{\sigma}(\omega) = \sigma_1 + i\sigma_2$ is complex effective conductivity of the metasurface given σ_1 and σ_2 as the real and imaginary part respectively, and Z_0 = 377 Ω is the impedance in free space. Although effective sheet conductivity $d\tilde{\sigma}(\omega)$ decreases with increasing temperature, the type and concentration of carriers contributing to the sheet conductivity are different under forward and reverse bias. This resluts in the bias polarity dependnece of the tranmission. At impedance matching (IM) condition, transmission has a theoretical maximum $\frac{E_{Si+coating}(\omega)}{E_{Si}(\omega)}\Big|_{IM} = abs\left(\frac{n_{air}+n_{Si}}{2n_{Si}+jZ_0 d\sigma_2(\omega)}\right)$, which is only dependent on the imaginary part of the complext effective conductivity.[22] As the carrier type and concentration is different under reverse and forward bias, the effective terahertz conductivity of the silicon metasurface especially the imaginary part changes. Therefore, the active silicon metasurface has a unique property that it thermally tunes the reflection and electrically tunes transmission.

In conclusion, we have demonstrated an electrical bias voltage controlled silicon metasurface for broadband terahertz antireflection application. The reflection coefficient can be continuously tuned and precise antireflection condition can be achieved. The transmission of THz wave through the silicon metasurface shows a unique dependence on bias voltage

polarity. The tuning range in transmission can be expanded by improving design of the junction region as well as magnifying the electrical tuning while reducing the thermal tuning. Further exploitation on independently biasing the *p*-*n* junctions or designing modular functions may lead to programmable metamaterials and metasurfaces proposed recently.[23] The CMOS compatibility and smooth nature of the metasurface could potentially facilitate monolithic integration with other planar optical components for applications in terahertz and other frequency regime. It also links active metasurface research with existing silicon integrated photonic architectures,[24] which would bring new possibility to realize novel and complex optical systems using metasurfaces.

Experimental Section

Device fabrication: The interdigitated p-n junction diodes are fabricated on an 8 inches silicon wafer through standard CMOS process in IME's (Institute of Microelectronics, Agency for Science, Technology and Research (A*STAR)) silicon photonics line.[25] The wafer is double side polishing and has a thickness of 725 ± 15 µm. It is slightly p-doped with Boron with bulk resistivity of $\rho_{substrate}$ = 5 KΩ·cm. The p-n junction is formed by using standard implantation with Boron and Phosphorus as the dopants respectively. Period Λ is 5 µm and width W is 2.5 µm (**Figure 1**b). Doping concentrations of *p*++ and *n*++ Ohmic contacts are higher than 1×10^{20} cm^{-3}. Rapid thermal annealing is applied to activate the dopants. A 500 nm cladding oxide is deposited by plasma-enhanced chemical vapor deposition, followed with contact hole opening to *p*++ and *n*++ regions. Aluminum with 750 nm in thickness is deposited and patterned to form the contact pads. The cladding oxide is completely etched in the interdigitated *p*-*n* area to form a terahertz transmission window of 5×5 mm^2. Finally, the wafer is mechanically diced and individual device is wire-bonded for electrically testing.

Mid-infrared near-field imaging: Near field images are obtained by a commercial s-SNOM (Neaspec GmbH) (Supporting Information, Figure S2). Scanning area is 10×5 μm by 600×100 pixels. The experiment is performed at ambient conditions.

Bias-voltage-dependent THz-TDS spectroscopy: The measurement uses a commercial terahertz system (Menlo TERA-K15) (Supplementary Information, Figure S3).

Passive THz-TDS spectroscopy: The measurement uses a commercial terahertz system (TPS Spectra 3000) (Supporting Information, Figure S4).

Voltage-temperature measurement: Surface temperature of the biased sample is measured by a contact thermometer (TKDT 10), while sample is mounted in the same way as in bias-voltage-dependent THz-TDS measurement.

Supporting Information,
Supporting Information, is available from the Wiley Online Library or from the author.

Acknowledgement

The authors thank J.N.Wang for valuable discussions on the device transport physics, D.V.M.Repaka, H.K.Ng, K.Hippalgaonkar, H.W.Liu, N.Zhang and L.Ke for sharing tools for the device characterization, A.Cernescu for discussions and technical support on the use of MIR s-SNOM, and C.M.Ke for discussion on device simulation. The work was financially supported by the Institute of Materials Research and Engineering and the Agency for Science, Technology and Research (A*STAR) under Grant No. 152 7000014.

Received: ((will be filled in by the editorial staff))
Revised: ((will be filled in by the editorial staff))
Published online: ((will be filled in by the editorial staff))

References

[1] a) M. Tonouchi, *Nat. Photon.* **2007**, *1*, 97; b) X. C. Zhang, A. Shkurinov, Y. Zhang, *Nat. Photon.* **2017**, *11*, 16.
[2] a) C. L. Holloway, E. F. Kuester, J. A. Gordon, J. O'Hara, J. Booth, D. R. Smith, *IEEE Antennas Propag. Mag.* **2012**, *54*, 10; b) H.-T. Chen, A. J. Taylor, N. Yu, *Rep. Prog. Phys.* **2016**, *79*, 076401.

[3] M. Rahm, J.-S. Li, W. J. Padilla, *J. Infrared Millim. Terahertz Waves.* **2013**, *34*, 1.
[4] T. Kleine-Ostmann, P. Dawson, K. Pierz, G. Hein, M. Koch, *Appl. Phys. Lett.* **2004**, *84*, 3555.
[5] H.-T. Chen, W. J. Padilla, M. J. Cich, A. K. Azad, R. D. Averitt, A. J. Taylor, *Nat. Photon.* **2009**, *3*, 148.
[6] S. H. Lee, M. Choi, T.-T. Kim, S. Lee, M. Liu, X. Yin, H. K. Choi, S. S. Lee, C.-G. Choi, S.-Y. Choi, *Nat. Mater.* **2012**, *11*, 936.
[7] J. Han, A. Lakhtakia, *J. Mod. Opt.* **2009**, *56*, 554.
[8] L. Kang, Q. Zhao, H. Zhao, J. Zhou, *Opt. Express* **2008**, *16*, 17269.
[9] I. H. Libon, S. Baumgärtner, M. Hempel, N. Hecker, J. Feldmann, M. Koch, P. Dawson, *Appl. Phys. Lett.* **2000**, *76*, 2821.
[10] a) H.-T. Chen, J. F. O'Hara, A. K. Azad, A. J. Taylor, R. D. Averitt, D. B. Shrekenhamer, W. J. Padilla, *Nat. Photon.* **2008**, *2*, 295; b) L. Deng, J. Teng, H. Liu, Q. Y. Wu, J. Tang, X. Zhang, S. A. Maier, K. P. Lim, C. Y. Ngo, S. F. Yoon, *Adv. Opt. Mater.* **2013**, *1*, 128.
[11] D. R. Chowdhury, R. Singh, J. F. O'Hara, H.-T. Chen, A. J. Taylor, A. K. Azad, *Adv. Opt. Mater.* **2011**, *99*, 231101.
[12] a) H. Tao, A. C. Strikwerda, K. Fan, W. J. Padilla, X. Zhang, R. D. Averitt, *Phys. Rev. Lett.* **2009**, *103*, 147401; b) S. M. Kamali, E. Arbabi, A. Arbabi, Y. Horie, A. Faraon, *Laser Photon. Rev.* **2016**, *10*, 1002; c) B. Gupta, S. Pandey, A. Nahata, T. Zhang, A. Nahata, *Adv. Opt. Mater.* **2017**, *5*, 1601008.
[13] H.-T. Chen, W. J. Padilla, J. M. Zide, A. C. Gossard, A. J. Taylor, R. D. Averitt, *Nature* **2006**, *444*, 597.
[14] a) I. Staude, J. Schilling, *Nat. Photon.* **2017**, *11*, 274; b) M. R. Hashemi, S. Cakmakyapan, M. Jarrahi, *Rep. Prog. Phys.* **2017**, *80*, 094501.
[15] a) H.-T. Chen, J. Zhou, J. F. O'Hara, F. Chen, A. K. Azad, A. J. Taylor, *Phys. Rev. Lett.* **2010**, 105, 073901; b) H.-T. Chen, C.-C. Chang, L. Huang, presented at 42nd IRMMW-THz, Mexico, Aug. **2017**.
[16] a) L. Ding, Q. Y. S. Wu, J. F. Song, K. Serita, M. Tonouchi, J. H. Teng, *Adv. Opt. Mater.* **2013**, *1*, 910; b) L. Ding, Q. Y. S. Wu, J. H. Teng, *Laser Photon. Rev.* **2014**, *8*, 941.
[17] K. Wang, D. M. Mittleman, *Nature* **2004**, *432*, 376.
[18] J. Dai, J. Zhang, W. Zhang, D. Grischkowsky, *J. Opt. Soc. Am. B* **2004**, *21*, 1379.
[19] A. J. Huber, D. Kazantsev, F. Keilmann, J. Wittborn, R. Hillenbrand, *Adv. Mater.* **2007**, *19*, 2209.
[20] A. Thoman, A. Kern, H. Helm, M. Walther, *Phys. Rev. B* **2008**, *77*, 195405.
[21] H. Li, *J. Phys. Chem. Ref. Data* **1980**, *9*, 561.
[22] G. Jnawali, Y. Rao, H. Yan, T. F. Heinz, *Nano Lett.* **2013**, *13*, 524.
[23] a) T. J. Cui, M. Q. Qi, X. Wan, J. Zhao, Q. Cheng, *Light Sci. Appl.* **2014**, *3*, e218; b) S. Liu, T. J. Cui, Q. Xu, D. Bao, L. Du, X. Wan, W. X. Tang, C. Ouyang, X. Y. Zhou, H. Yuan, *Light Sci. Appl.* **2016**, *5*, e16076; c) S. Liu, T. J. Cui, L. Zhang, Q. Xu, Q. Wang, X. Wan, J. Q. Gu, W. X. Tang, M. Qing Qi, J. G. Han, *Adv. Sci.* **2016**, *3*, 1600156; d) S. Liu, T. J. Cui, *Adv. Opt. Mater.* **2017**, *5*, 1700624; e) A. Nemati, Q. Wang, M. H. Hong, J. H. Teng, *Opto-Electron. Adv.* **2018**, *1*,180009.
[24] A. W. Poon, X. Luo, F. Xu, H. Chen, *Proc. IEEE* **2009**, *97*, 1216.
[25] A. E.-J. Lim, J. Song, Q. Fang, C. Li, X. Tu, N. Duan, K. K. Chen, R. P.-C. Tern, T.-Y. Liow, *IEEE J. Sel. Topics Quantum Electron.* **2014**, *20*, 405.

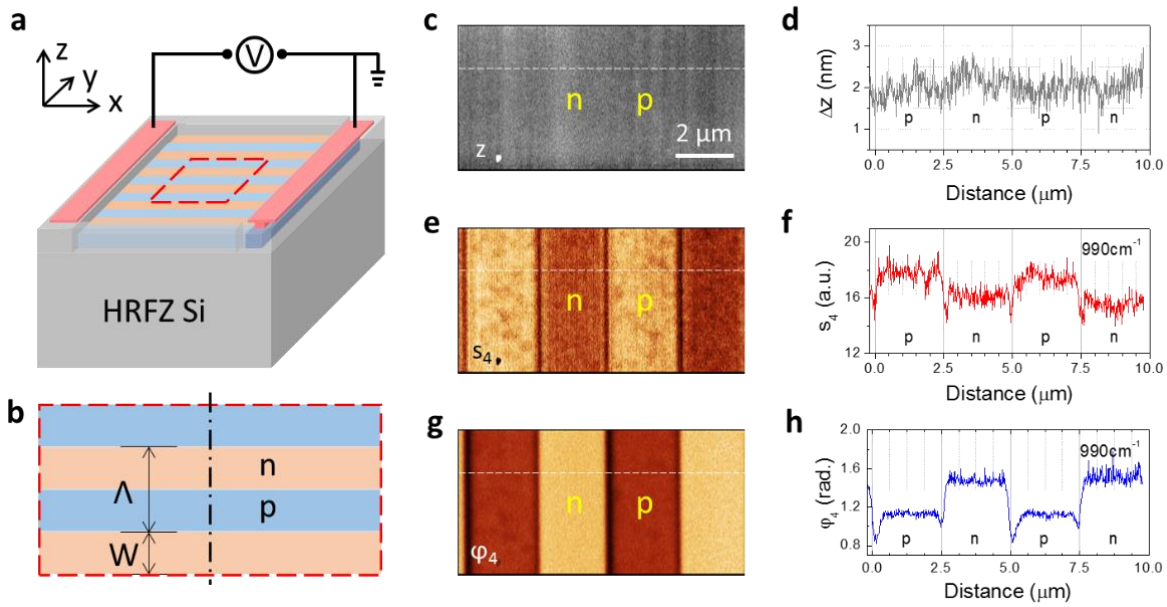

Figure 1. a) Schematic of the device. b) Zoom-in top view of the silicon metasurface. Λ is the period and W is the width of the *p*-/*n*-type silicon stripe. c-h) Real-space mid-infrared s-SNOM imaging of the silicon metasurface taken in a single scan at wavenumber 990 cm^{-1}. AFM topographic image (c) and a line plot (d) extracted from the dashed line in (c). Optical amplitude signal s_4 of the interdigitated *p*-*n* junctions (e) and a line plot (f) extracted from the dashed line in (e). Optical phase signal φ_4 of the interdigitated *p*-*n* junctions (g) and a line plot (h) extracted from the dashed line in (g). The *p*- and *n*-type regions are identified by correlating the scanning images with the mask design.

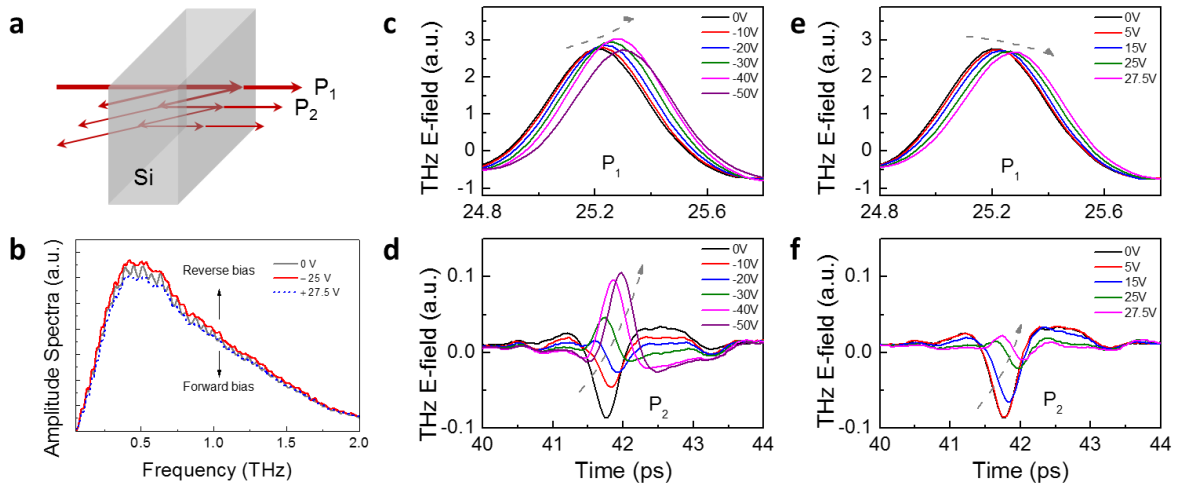

Figure 2. a) Schematic of multiple reflections between the air-silicon interfaces. b) Terahertz amplitude spectra at selected bias voltages. c-d), Time-domain traces of main pulse P_1 (c) and the first echo P_2 (d) under reverse bias. e-f), Time-domain traces of main pulse P_1 (e) and the first echo P_2 (f) under forward bias.

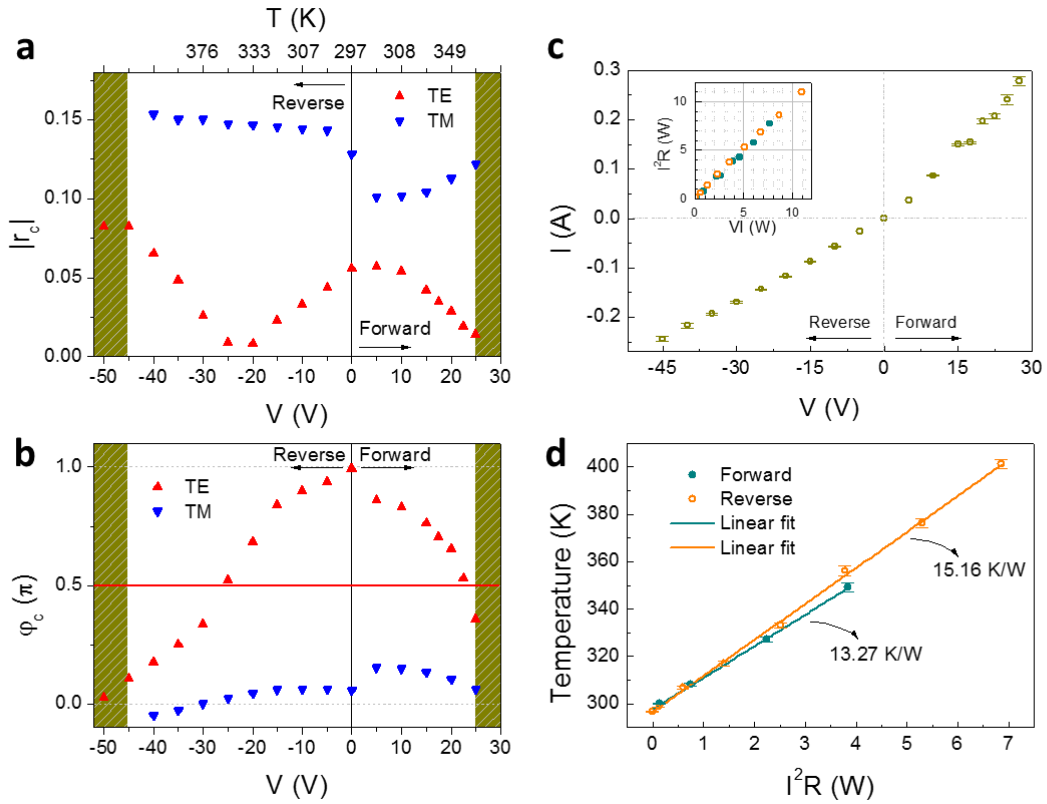

Figure 3. a,b) Bias voltage and surface temperature dependent complex reflection coefficient of silicon metasurface at 1.1 THz in TE and TM configurations, amplitude $|r_C|$ (a) and phase φ_C (b). c) *IV* result of the active silicon metasurface. Inset plots the electric power conversion relation. d) Surface temperature as a function of dissipated electric power.

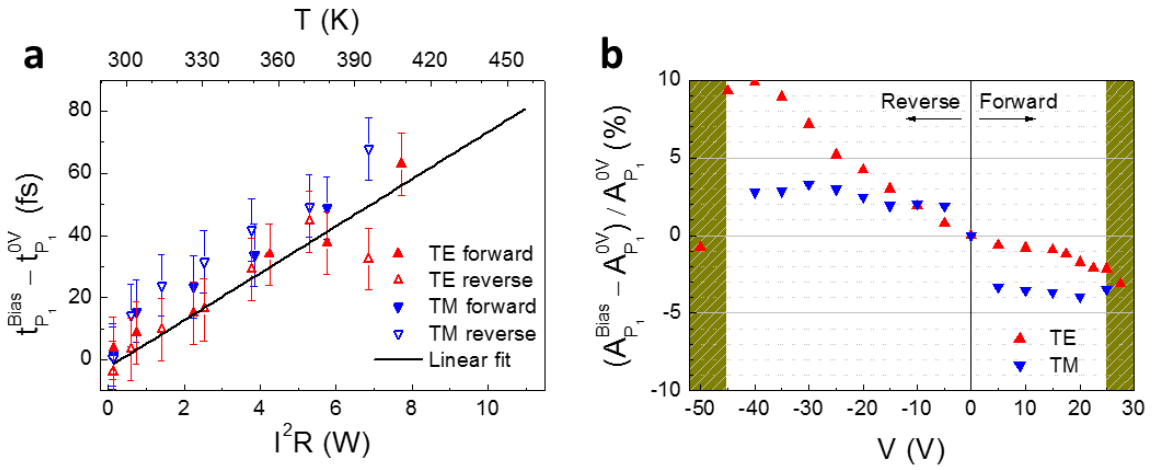

Figure 4. a) Relative time delay of P_1 as a function of dissipated power (I^2R) under forward and reverse bias with respect to that of zero bias in TE and TM configurations. A linear fit with slope $\partial t/\partial P$ = 7.5 fs/W is superimposed. The corresponding surface temperature is indicated in the upper X axis. b) Normalized amplitude variation of P_1 with respect to that of zero bias in TE and TM configurations.

((Supporting Information can be included here using this template))

Supporting Information

Electrically and Thermally Tunable Smooth Silicon Metasurfaces for Broadband Terahertz Antireflection

Lu Ding[*], *Xianshu Luo, Liang Cheng, Maung Thway, Junfeng Song, Soo Jin Chua, Elbert E. M. Chia, Jinghua Teng*[*]

S1. Ion implantation profile

A thin layer of silicon is doped with Boron or Phosphorus, for p- or n-type doping respectively, by ion implantation. Depth profile of the doping concentration of the selected sample is measured by dynamic secondary ion mass spectrometry (D-SIMS) (Fig. S1). Boron has a concentration ~4×10^{19} cm^{-3} uniformly distributed in the first 100 nm and exponentially decreases to 1×10^{16} cm^{-3} until depth of 550 nm. Phosphorus has a higher concentration of ~7×10^{19} cm^{-3} uniformly distributed in the first 50 nm depth and faster exponentially decreases to 2×10^{16} cm^{-3} until depth of 450 nm. Analytical error is estimated about 5%~10%. Implantation depth is much smaller than the wavelength of terahertz wave. For antireflection based on impedance matching, the surface of silicon substrate shall have a thin conductive layer with critical sheet conductivity of $d\sigma_{dc}$ = 6.42 mS.[1] Here, the doping concentration is purposely chosen to give rise to a higher effective sheet conductivity than the critical value, so that the impedance of air is over compensated for later active tuning purpose.

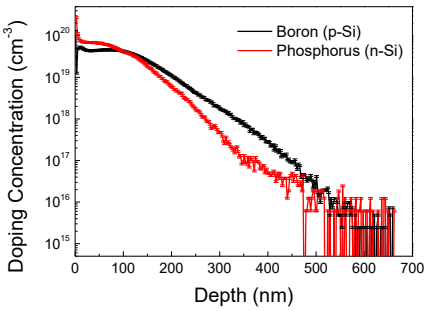

Fig. S1. Depth profile of p- and n-Si doping measured by D-SIMS.

S2. Mid-infrared near-field imaging

The detection scheme of mid-infrared near-field imaging by s-SNOM is shown in Fig. S2. It is based on an AFM operating in tapping mode at frequency of $\Omega \approx 250$ kHz and a tapping amplitude of 70 nm. The spatial resolution is about 25 nm defined by the radius of curvature of the AFM tip apex. Mid-infrared laser source is a quantum cascade laser operating at 990 cm^{-1}. A pseudo-heterodyne interferometric detection module is implemented in the s-SNOM to extract both the scattering amplitude (s) and phase (φ) of the near-field signal. To subtract the background signal, we demodulated the near-field signal at the fourth harmonics 4Ω of the tapping frequency. Here, both s_4 and φ_4 signals are as-measured since they are sufficient to describing all the doping characteristics of the silicon metasurface.

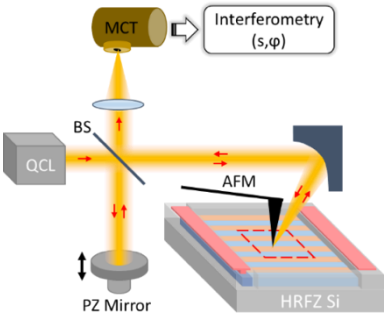

Fig. S2. Schematics of mid-infrared near-field imaging using s-SNOM.

S3. Bias-voltage-dependent THz-TDS spectroscopy

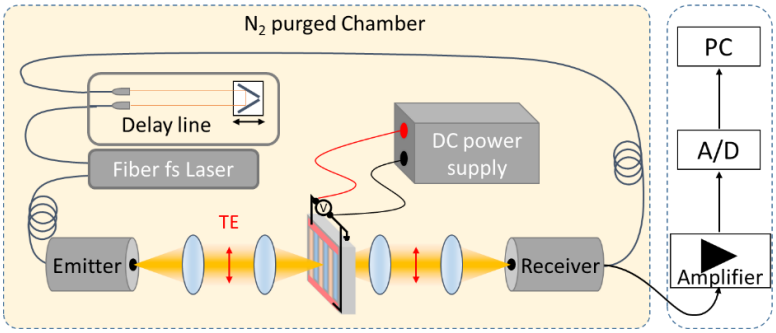

Fig. S3. Schematics of bias-voltage-dependent THz-TDS using Menlo TERA K15.

The experiment is carried out using a commercial terahertz system (Menlo TERA K15), shown in Fig. S3. THz beam is vertically polarized with the spectral range from 0.1 to 3 THz. THz beam is focused on sample via TPX50 lens with 50 mm effective focal length. The system is in an enclosure purged with N_2 gas to avoid the absorption from atmospheric water vapor. The device is centered and glued on an aluminum holder with a hole (diameter is 4 mm). The electrodes of the device are wire bonded to a customized PCB board for supplying bias voltage though a DC power supply (HP 6633A 0 – 50 V / 0 – 2 A). The transmitted time signal is integrated 20 s to improve the signal-to-noise ratio.

S4. Passive THz-TDS spectroscopy

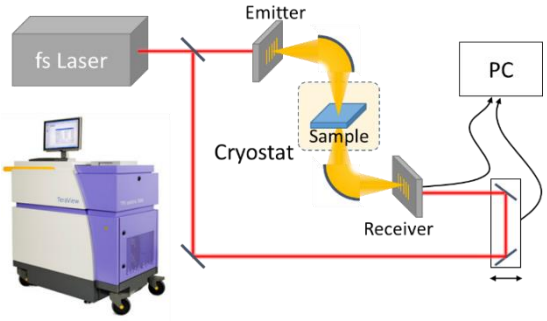

Fig. S4. Schematics of passive THz-TDS system using TPS Spectra 3000.

Passive THz TDS experiment uses a commercial terahertz system (TPS Spectra 3000) as shown in Fig. S4. THz beam is linearly polarized in vertical direction with the spectral range from 0.1 to 3 THz. The beam is focused on sample by a parabolic mirror with a divergence angle of 2.5/8. The sample is mounted on the cold finger of a Janis cryostat with the doped side

in contact with the cold finger. The chamber is vacuumed using a mechanical pump (IDP-3) to avoid the absorption from atmospheric water vapor. Temperature range is from 300 to 350 K, which is controlled by Lakeshore 332 temperature controller. The acquired data are averaged from 900 spectra with a scanning frequency of 30 Hz, which gives a very high signal to noise ratio. Spectral resolution is 0.06 THz.

S5. Passive THz-TDS at room temperature

Fig. S5a shows complete time domain traces of air, silicon, silicon with p-Si thin layer, silicon with n-Si thin layer, and silicon metasurface in TE and TM configurations (TPS Spectra 3000). Pulse profile of free space terahertz pulse is maintained in silicon, p-Si, n-Si, and silicon metasurface in TE configuration. Fig. S5b plots the transmission spectra of P_1 normalized to that of silicon. The broadband nature of p-Si, n-Si, and silicon metasurface in TE configuration is shown since the normalized transmission are flat over the entire spectral range. Fig. S5c shows the amplitude $|r_C|$ of the complex reflection coefficient. Up on the general broadband feature of $|r_c|$, there are oscillations more and more significant when $|r_c|$ gets close to zero or to frequency extremes of the THz-TDS system. Such oscillations are also observed in transmission spectra (Fig. S5b) at frequency extremes of the THz-TDS system. We attribute the oscillations in reflection and transmission spectra to the bad signal-to-noise ratio when very close to the frequency extremes of the THz-TDS system as well as the weak signal of P_2 near complete antireflection condition.

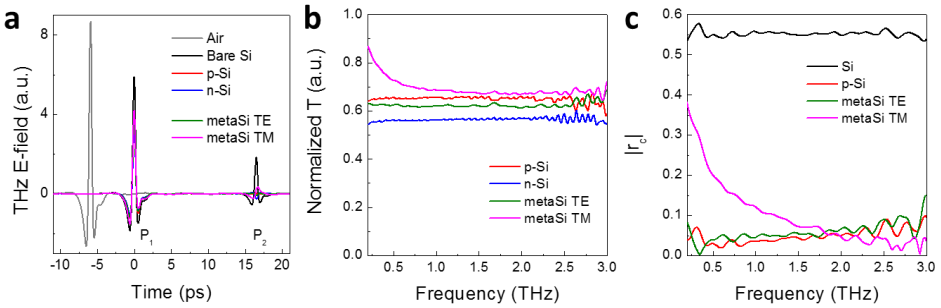

Fig. S5. a) Time domain traces of air, silicon, silicon with p-Si thin layer, silicon with n-Si thin layer, and silicon metasurface in TE and TM configurations (TPS Spectra 3000). b) Transmission spectra of P_1 normalized to that of silicon. c) $|r_C|$ in frequency domain of silicon, silicon with p-Si thin layer, and silicon metasurface in TE and TM configurations.

Silicon (black curve) has strong P_2 due to its high refractive index. The reflection coefficient calculated by $r = \sqrt{P_2/P_1} = 0.55$ agrees well with that calculated by the Fresnel equation $\frac{n_{Si}-n_{air}}{n_{Si}+n_{air}} = 0.547$, taking n_{Si} = 3.4175 and n_{air} = 1.0003.[2] For p-Si (red curve), P_1 is reduced to 65% attributed to free carrier absorption, while P_2 is almost vanished due to nearly impedance matching. For n-Si (blue curve), P_1 is reduced further to 56% and P_2 has inverted phase due to impedance over compensation. Interestingly, it is the doping concentration determines the terahertz response rather than the type of dopant, considering the very similar response of p-Si and n-Si.

For silicon metasurface, in TE configuration (green curve), P_1 is reduced to 62.3% and P_2 is inverted. In TM configuration (magenta curve), not only the amplitude of P_1 is reduced but also the pulse profile is modified. Transmission monotonically decreases to 68% with increasing frequency and remains at a constant at high frequency (Fig. S5b). It is because that the depletion region between p-n junctions acts as an effective gap to stop the free movement of the carriers from adjacent doped regions in TM configuration, which is similar to the case of

metal grating.[3] However, the p- and n-type regions are physically close where the depletion region is only a few hundreds of nanometers (Fig. 1h). Such periodicity modifies the transmitted pulse profile and the frequency response in TM configuration. It is qualitatively verified by the FDTD simulation in which the electronic property of individual doped silicon is extracted from Fig. S5a.

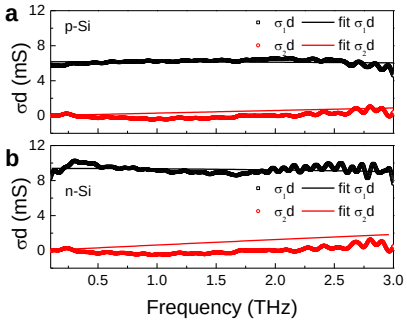

Fig. S6. Complex sheet conductivity of a) p-Si and b) n-Si thin layer. Both real and imaginary part of sheet conductivity are fit by Drude model.

The complex sheet conductivity $d\tilde{\sigma}(\omega) = d\sigma_1 + id\sigma_2$ of p-/n-Si thin layer is calculated by comparing the time-dependent electric field of terahertz pulse transmitted through the thin film sample as well as through the uncoated substrate as reference.[4]

$$\frac{E_{Si+film}(\omega)}{E_{Si}(\omega)} = \frac{n_{air} + n_{Si}}{n_{air} + n_{Si} + Z_0 d\tilde{\sigma}(\omega)}, \quad \text{(S1)}$$

where $Z_0 = \sqrt{\mu_0/\varepsilon_0} = 377\Omega$ is the impedance of free space. Due to the complexity of the doping profile, only the sheet conductivity is meaningful. Results are plot in Figs. S6a,b. $d\sigma_{dc}$ is extrapolated to be 6.35 and 9.42 mS for p- and n-Si samples respectively. P-Si thin layer is very close to the impedance matching condition ($d\sigma_{dc}$ = 6.42 mS), while n-Si thin layer is over compensated. $d\sigma_{dc}$ of p- and n-Si thin layer is also measured by Van der Pauw (VdP) method to be 6.64 ± 0.02 and 9.68 ± 0.02 mS, respectively. The wafer level uniformity for p- and n-Si is 6.8 ± 0.3 and 9.9 ± 0.3 mS, respectively. Results from both experiments agree well with each other.

The complex conductivity of doped silicon calculated by Eq. (S1) is fit by Drude model[5] $\tilde{\sigma}(\omega) = \frac{\varepsilon_0 \omega_p^2 \tau}{1 - i\omega\tau}$, where the plasma frequency ω_p is given by $\omega_p^2 = Ne^2/\varepsilon_0 m^*$; N is the carrier density, m^*=0.26m_0 for the effective electron mass and 0.37m_0 for the effective hole mass;[6] m_0 is the free electron mass. The relaxation time τ is given by $\mu = |e|\tau/m^*$; μ is the electron or hole mobility which is the key fitting parameter. Carrier density is taken from DSIMS results (Fig. S1). The fitting electron mobility is 73.9 $cm^2V^{-1}S^{-1}$ and hole mobility is 53.3 $cm^2V^{-1}S^{-1}$, which agrees nicely with literature.[7] Fitting curves show fairly good agreement with experiment. Discrepancy on the imaginary part at high frequency is attributed to the simple model which neglecting the complexity on non-uniform depth profile of doping. Validity of Drude model confirms that doped silicon is metalized for current doping condition. The electronic property of doped silicon thin layer is summarized in Table S1.

Table S1. Electronic property of doped silicon thin layer

Element	Type of Dopant	Doping Concentration (D-SIMS) x 10^{14} cm^{-2}	$d\sigma_1$ (VdP) mS	$d\sigma_1$ (TDS) mS	Mobility (fitting) $cm^2V^{-1}s^{-1}$
Boron	p	7.23	6.64±0.02	6.35	53.3
Phosphorus	n	7.93	9.68±0.02	9.42	73.9

Fig. S7 compares the FDTD simulation (Lumerical FDTD) result with experiment. Fig. S7a shows refractive index profile of silicon and silicon metasurface in one period. Periodic boundary condition is applied in X direction and PML on Z direction. A plain wave source is applied with frequency span from 0.5-3 THz and propagates along Z axis. Mesh is auto non-uniform and minimum mesh step is 0.25 nm. An additional mesh is added to the doping layer with dx=50nm, dy=1um, and dz=50nm. Auto shutoff minimum is 5e-6 and simulation time is 100 ps. For the simplicity of simulation, we used the default pulse setting. A few approximations are taken in the simulation: the doped silicon layer has constant doping over 500 nm; the depletion region is replaced by intrinsic silicon; and the gap between doped silicon is 200 nm. Fig. S7b shows normalized FDTD time domain traces of silicon and silicon metasurface in TE and TM configurations. The pulse profile in TM configuration is indeed modified. The frequency dependence of experimental and simulated transmission spectra has shown qualitative similarity, seen in Figs. S7c,d. Given above simulation condition, the simulation results are good enough for qualitative comparison with experiment.

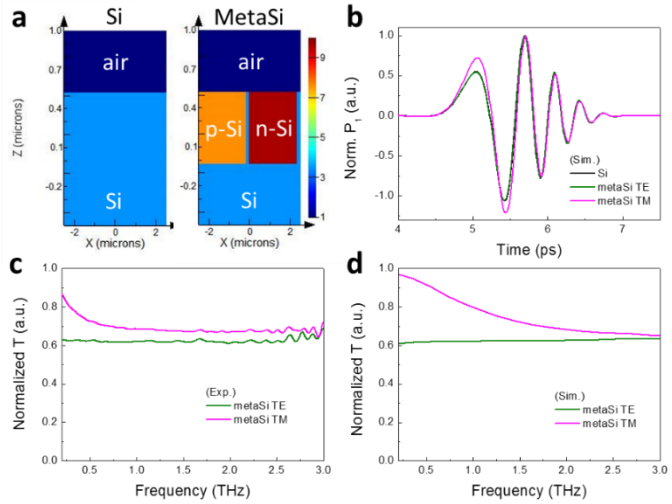

Fig. S7. a) FDTD refractive index profile of silicon and silicon metasurface in one period. b) Normalized FDTD time signal of silicon and silicon metasurface in TE and TM configurations. c,d) Experimental (c) and simulated (d) normalized transmission spectra calculated by FFT.

S6. Passive THz-TDS at high temperature

Temperature dependent THz-TDS measurement (TPS Spectra 3000) is carried out to understand the thermal influence on bias-voltage-dependent THz-TDS results. Time signals are compared between silicon, silicon with p-Si thin layer, and silicon metasurface in TE and TM configurations. Two distinct temperatures are selected 300 and 350 K. Higher temperature is not achievable due to the limitation of heating unit.

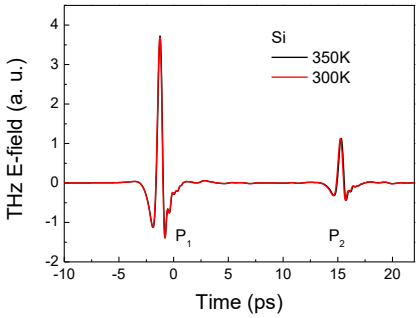

Fig. S8. Experiment time domain traces for silicon at 300 and 350 K.

In silicon, heating results in a pure time delay of the terahertz pulses (Fig. S8). P_1 and P_2 shift laterally by +23 and +67 fs respectively for a temperature increment of ΔT=50 K. The refractive index of silicon increases at a rate of $(1/n)(dn/dT) = 4.8\times10^{-5}$ K^{-1} which agrees well with the published results.[8] It results in an insignificant change in reflection coefficient (~10^{-3}) at Si/air interface.

In silicon with p-Si thin layer, heating not only results in time delay for P_1 but also increases its amplitude (Fig. S9a). Time delay is attributed to the slightly refractive index change in the silicon substrate. Increasing amplitude means decreasing real sheet conductivity of the doped layer, calculated as -0.28 mS for ΔT=50 K. The reflection coefficient at Si/p-Si/air interface is totally changed by 22.2×10^{-3} which is one order of magnitude higher than that of silicon. Therefore, if one purposely dopes silicon thin layer to overcompensate the impedance mismatch between silicon and air, impedance matching can be achieved by increasing temperature and the total transmission will increase. FDTD simulation is carried out on a similar structure. Fig. S9b is the refractive index profile of air/p-Si/Si at 300 and 400 K. Fig. S9c shows simulation results in time domain. The amplitude of pulse increases as expected.

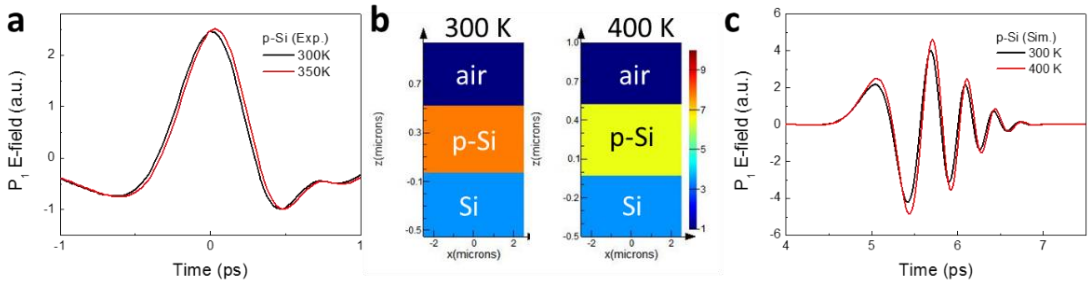

Fig. S9. a) Experiment time domain traces for p-Si at 300 and 350 K. b) Refractive index profile of air/p-Si/Si at 300 and 400 K. c) FDTD results for p-Si at 300 and 400 K.

Fig. S10 plots the experimental and simulated temperature dependent THz-TDS results on silicon metasurface. In TE configuration, it has the same trend as that of p-Si. The calculated reflection coefficient of silicon metasurface is in total changed by 26.3×10^{-3} which is comparable with that of p-Si. In TM configuration, amplitude of P_1 has non-uniform increment comparing to TE configuration. Simulation and experiment agree well with each other despite that THz pulse profiles are different.

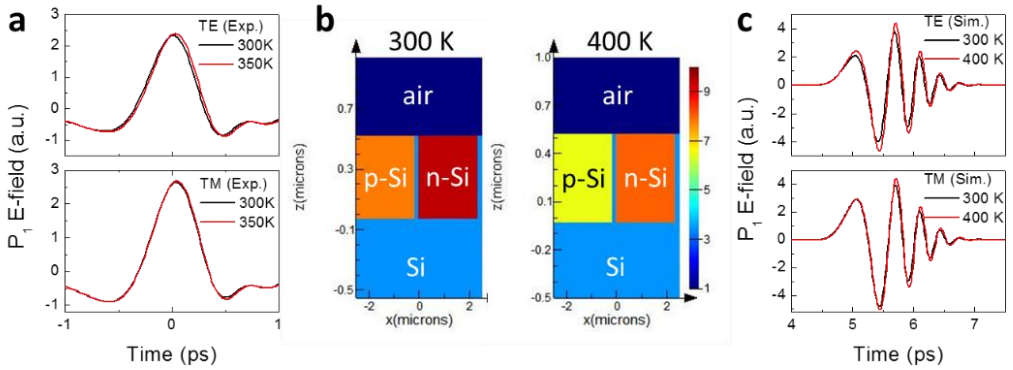

Fig. S10. a) Experiment time domain traces (TE/TM) for silicon metasurface at 300 and 350 K. b) Refractive index profile of air/metaSi/Si at 300 and 400 K. c) FDTD results for silicon metasurface at 300 and 400 K.

S7. Temperature dependence of $|r_C|$ of silicon metasurface

The temperature dependence of complex reflection coefficient r_C of silicon metasurface can be further understand analytically using effective medium model,[3] *e. g.* a three-layered system where metasurface structure is sandwiched between two dielectric media with different refractive indices. The schematics is shown in Fig. S11a. Only TE configuration is considered. Periodic and electromagnetic boundary conditions are applied to the electric and magnetic fields of the propagating terahertz wave in three individual layers along the OX and OZ directions, respectively. As a test of principle, the antireflection coating is only n-doped. Filling factor is f = 0.9. Taking doping concentration and mobility from Table S1 and considering the fact that high temperature mobilities are limited by phonon scattering $\mu_{ph} \sim T^{-3/2}$, the calculated reflection coefficient is shown in Fig. S11b. $|r_C|$ has clear temperature dependence due to the temperature dependent conductivity. Interestingly, it cannot reach absolute zero. Fig. S11b inset shows the real $\mathrm{Re}(r_C)$ and imaginary $\mathrm{Im}(r_C)$ part of the reflection coefficient near the impedance matching point. It shows a finite $\mathrm{Im}(r_C)$ when $\mathrm{Re}(r_C)$ =0, which is due to the finite imaginary part of the complex conductivity.

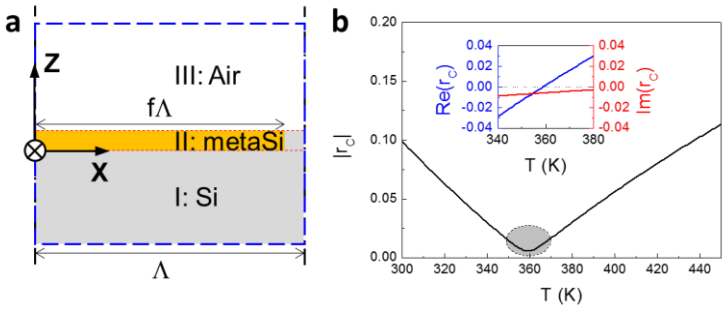

Fig. S11. a) Schematics of simulation geometry. b) Theoretically calculated $|r_C|$ as a function of temperature at 1 THz. Inset shows real $\mathrm{Re}(r_C)$ and imaginary $\mathrm{Im}(r_C)$ near the impedance matching point.

S8. Transmission THz-TDS in TM configuration of active silicon metasurface

The device is mounted in TM configuration, where the longer side of silicon stripe is perpendicular to the polarization of the incident THz wave (Fig. S12a). P_1 and P_2 (Figs. S12b,c respectively) show the same waveform which is slightly modified comparing with that of silicon (Fig. S3a inset). Amplitude of P_1 and P_2 are bias-polarity dependent and the phase are delayed. The amplitude are calculated by FFT of the temporal waveform of the detected terahertz pulses which show strong interference fringes spectra (Fig. S12d). Therefore, in TM configuration, the silicon metasurface has tunability on terahertz amplitude and phase irrelevant to antireflection property.

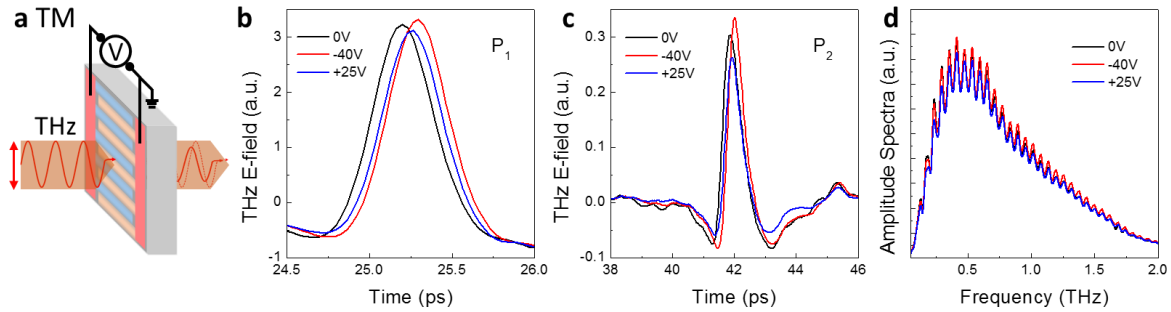

Fig. S12. a) Schematic of transmission THz-TDS in TM configuration. b-d) Time-domain traces of main pulse P_1 (b) and the first echo P_2 of the silicon substrate (c) at selected bias voltages, and amplitude spectra calculated by FFT (d).

S9. Modulation of active silicon metasurface

The setup for electrical modulation experiment is shown in Fig. S13a. The DC power supply is set at 35 V. When applying bias voltage to the device, a Songle relay (maximum electrical switching frequency is 0.5 Hz) is wired between the DC power supply and the device in series configuration to switch bias between ON and OFF states. Switching frequency is controlled by a function generator which generates a TTL square wave between 0 and 5 V. The device is thus periodically reverse-biased between 0 and -35 V. Then, THz transmission pulse trains under modulated bias is monitored by an oscilloscope. Transmission peak intensity is extracted and normalized between 0 and 1, where 0 represents the static transmission level at 0V and 1 represents the static transmission level at -35 V. Fig. S13b plots the normalized transmission modulated at 0.1 Hz, 0.3 Hz, 0.5 Hz, and 0.7 Hz. At 0.1 Hz, the intensity increases/decreases when switching ON/OFF the reverse bias, respectively. After switching, the intensity takes about 2 s to stabilize. Since the modulation frequency is slower than the maximum switching frequency of the relay, the measured result is true device response. With increasing modulation frequency, the device shows obvious retardation at the rising and falling edges, and the amplitude cannot reach maximum before the circuit open. Slow modulation speed indicates that the nature of modulation is thermally based, which is due to the large size of the device and the inefficient heat dissipation via air. Therefore, the current device is only suitable for 'quasi-static' tuning.

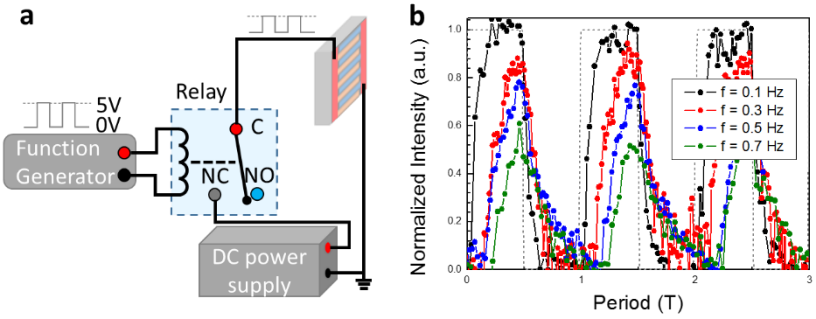

Fig. S13. a) Schematic of electrical modulation setup. A relay is wired in series configuration between DC power supply and the device to switch ON/OFF the voltage. C, NC, and NO are short for common, normally closed, and normally open. b) Normalized transmission modulated at various frequency.

Supplementary References

[1] A. Thoman, A. Kern, H. Helm, M. Walther, *Phys. Rev. B* **2008**, *77*, 195405.
[2] J. Dai, J. Zhang, W. Zhang, D. Grischkowsky, *J. Opt. Soc. Am. B* **2004**, *21*, 1379.
[3] L. Ding, Q. Y. S. Wu, J. F. Song, K. Serita, M. Tonouchi, J. H. Teng, *Adv. Opt. Mater.* **2013**, *1*, 910.
[4] M. Tinkham, *Phys. Rev.* **1956**, *104*, 845.
[5] a) T.-I. Jeon, D. Grischkowsky, *Phys. Rev. Lett.* **1997**, *78*, 1106; b) S. Nashima, O. Morikawa, K. Takata, M. Hangyo, *Appl. Phys. Lett.* **2001**, *79*, 3923.
[6] W. Spitzer, H. Fan, *Phys. Rev.* **1957**, *106*, 882.
[7] G. Masetti, M. Severi, S. Solmi, *IEEE Trans. Electron Devices.* **1983**, *30*, 764.
[8] H. Li, *J. Phys. Chem. Ref. Data* **1980**, *9*, 561.